The Influence of Meridional Gradients in Insolation and Long-Wave Optical Depth on the Climate of a Gray Radiation GCM

Nicholas J. Lutsko*

Department of Earth, Atmospheric, and Planetary Sciences, Massachusetts Institute of Technology, Cambridge, Massachusetts

Max Popp

Laboratoire de Météorologique Dynamique, Sorbonne Université, Paris, France

**Corresponding author address:* Nicholas Lutsko, Department of Earth, Atmospheric, and Planetary Sciences, Massachusetts Institute of Technology, Cambridge, Massachusetts

E-mail: lutsko@mit.edu

ABSTRACT

The relative contributions of the meridional gradients in insolation and in long-wave optical depth (caused by gradients in water vapor) to the equator-to-pole temperature difference, and to Earth's climate in general, have not been quantified before. As a first step to understanding these contributions, this study investigates simulations with an idealized general circulation model in which the gradients are eliminated individually or jointly, while keeping the global-means fixed. The insolation gradient has a larger influence on the model's climate than the gradient in optical depth, but both make sizeable contributions and the changes are largest when the gradients are reduced simultaneously. Removing either gradient increases global-mean surface temperature due to an increase in the tropospheric lapse rate, while the meridional surface temperature gradients are reduced.

"Global warming" experiments with these configurations suggest similar climate sensitivities, however the warming patterns and feedbacks are quite different. Changes in the meridional energy fluxes lead to polar amplification of the response in all but the setup in which both gradients are removed. The lapse-rate feedback acts to polar amplify the responses in the Earth-like set-up, but is uniformly negative in the other set-ups. Simple models are used to interpret the results, including a prognostic model that can accurately predict regional surface temperatures, given the meridional distributions of insolation and long-wave optical depths.

1. Introduction

The meridional gradients in insolation and in long-wave optical depth (due to gradients in water vapor) play central roles in Earth's climate. Together, these gradients are responsible for the equator-to-pole temperature difference which drives the large-scale dynamics of Earth's atmosphere: the Hadley circulation in the tropics and the baroclinic turbulence which characterizes atmospheric circulation in the mid-latitudes (e.g., Held (2000); Vallis (2006)). The equator-to-pole temperature difference also plays an important role in driving the circulation of the oceans, both directly through differential heating of the ocean surface, and indirectly by driving the atmospheric surface winds which force oceanic motions. However, the relative contributions of the meridional gradients in insolation and in long-wave optical depth to the equator-to-pole temperature difference, and to Earth's climate in general, are currently unknown, and are the subject of investigation here.

Many previous studies have investigated Earth-like climates with varied equator-to-pole temperature differences. For example, this temperature difference has been varied in idealized general circulation models (GCMs) to develop and test scaling laws for mid-latitude dynamics (e.g., Schneider and Walker (2006); O'Gorman and Schneider (2008a); Zurita-Gotor and Vallis (2011)) and to investigate the properties of tropical stationary waves (e.g., Arnold et al. (2010); Lutsko (2017)). A separate line of research has examined warmer climates than today with reduced equator-to-pole temperature gradients, such as were experienced at past times in Earth's history and may reappear in extreme future climate change scenarios (e.g., Huber and Sloan (2001); Abbot and Tziperman (2008); Caballero and Huber (2014); Popp et al. (2016)).

There has also been much interest recently in simulations with comprehensive climate models with uniform sea-surface temperatures, creating global Radiative-Convective Equilibrium (RCE) worlds. These simulations, which have been performed with both prescribed surface temperatures and with slab oceans, and typically without rotation, are taken as global analogues for the tropical atmosphere. Recent studies have focused on convective organization and related phenomena such as the Madden-Julian Oscillation in this configuration (e.g., Coppin and Bony (2015); Reed et al. (2015); Pendergrass et al. (2016)); the internal variability of these systems (Arnold and Randall (2015); Coppin and Bony (2017)); and the response of global RCE simulations to increased CO_2 concentrations (Popke et al. 2013). Global RCE simulations with rotation have recently been used to study tropical cyclones (Shi and Bretherton (2014); Merlis et al. (2016)), and several studies have investigated the structure of the Inter-Tropical Convergence Zone in global, rotating RCE simulations (Sumi (1992); Kirtman and Schneider (2000); Chao and Chen (2004)).

None of these studies have addressed how the meridional gradients in insolation and in long-wave optical depth combine to create the equator-to-pole temperature gradient seen on Earth, however. We address this basic question here by performing simulations with a gray-radiation GCM in which the gradients in insolation and in long-wave optical depth are eliminated individually or jointly. Gray-radiation GCMs have been shown to reproduce the main features of the atmospheric circulation on Earth (Frierson et al. 2006), and are therefore powerful tools for studying changes in the basic climate and in the large-scale circulation. Moreover, the radiation can be precisely controlled in these models. An example of this, which is relevant for our study, is that long-wave optical depths are prescribed, making it simple to eliminate this gradient. Conventionally, these models also do not include clouds, further simplifying the analysis. Many topics have been investigated in gray radiation models, including atmospheric eddy length scales, meridional energy transports, eddy kinetic energy, tropical precipitation, the Hadley circulation and the dynamics of the Intertropical Convergence Zone (e.g., Frierson et al. (2006); Frierson et al. (2007);

O'Gorman and Schneider (2008b); O'Gorman and Schneider (2008a); Schneider et al. (2010); Levine and Schneider (2015); Bischoff and Schneider (2016)).

We consider the effects of eliminating each of the gradients separately and of eliminating both gradients simultaneously, which produces an RCE world (rotation is still included), and focus on the temperature structure of these simulations. By comparing with an Earth-like control simulation, these simulations provide insight into the roles these two gradients play in setting up the climate that is experienced on Earth. The RCE simulation also provides context for interpreting the relevance of global RCE simulations with more comprehensive climate models for the real Earth. In addition, we test how the GCM's response to global warming-like forcings is affected by eliminating these gradients. Comparing the tropical responses to these forcings with the high latitude responses helps reveal the mechanisms responsible for the polar amplification of warming in this type of model. Finally, we note that our simulations are also potentially relevant for understanding the atmospheres of exoplanets, with high obliquity for instance, as well as for understanding the atmosphere of a snowball Earth, which would contain very little water vapor and so would have a much weaker long-wave optical depth gradient (e.g., Pierrehumbert (2005)).

In the following section we provide details on the model we have used and the experiments we have performed. After this the impacts of eliminating the gradients on the global-mean temperature of the model are discussed in section 3 and we then investigate the zonal-mean temperature structure in section 4. In section 5 we describe how the different configurations respond to global warming-like perturbations, before ending with a summary and conclusions (section 6).

2. Model and Experiments

The GCM is the idealized model first described by Frierson et al. (2006), which solves the primitive equations on the sphere and is forced by a gray radiation scheme. The GCM is coupled to a slab ocean of depth 1m, with no representation of ocean dynamics or sea ice, and the model includes the simplified Betts-Miller (SBM) convection scheme of Frierson (2007). A mixed-layer depth of 1m was used so that the model would spin up quickly, while leaving the resulting mean climate the same as for larger mixed layer depths. We show results using a convective relaxation time-scale τ_{SBM} of 2 hours and a reference relative humidity RH_{SBM} = 0.7, but sensitivity tests were conducted in which these two parameters were varied and the results are very similar to what is presented below (not shown). The boundary layer scheme is the one used by O'Gorman and Schneider (2008b). In every experiment the GCM was integrated at T85 truncation (corresponding to a resolution of roughly 1.4° by 1.4° on a Gaussian grid) with 30 vertical levels extending up to 16hPa, starting from a state with uniform SSTs. The simulations lasted for 1000 days, with averages taken over the final 700 days.

The radiative fluxes are calculated using the two-stream approximation assuming hemispheric isotropy, with a single band:

$$\frac{dU}{d\tau} = (U - B), \tag{1a}$$

$$\frac{dD}{d\tau} = (B - D), \tag{1b}$$

where U is the upward flux, τ is the optical depth, $B = \sigma T^4$ and D is the downward flux. This is the grey-gas approximation to the full radiative transfer equations. The boundary condition at the surface is $U[\tau(z=0)] = \sigma T_s^4$ and at the top of the atmosphere $D(\tau = 0) = 0$. The radiative heating in the temperature equation is

$$Q = -\frac{1}{c_p \rho}\frac{\partial}{\partial z}(U - D). \tag{2}$$

In the control set-up the incoming solar radiation takes the form

$$S_0(\phi) = S_{s,0}(1 + \Delta_s/4(1 - 3sin^2(\phi))), \tag{3}$$

where $S_{s,0}$ is the global-mean insolation (including the effect of surface albedo), Δ_s determines the meridional insolation gradient and ϕ is latitude. None of the simulations include a diurnal cycle. The long-wave optical depth is specified to approximate the effects of atmospheric water vapor (Frierson et al. 2006). At the surface this takes the form

$$\tau_0(\phi) = \tau_{0e} + (\tau_{0p} - \tau_{0e}) sin^2\phi, \tag{4}$$

where τ_{0e} is the surface value at the equator and τ_{0p} is the surface value at the pole. The long-wave optical depth is then

$$\tau(p,\phi) = \tau_0 \left[f_l \left(\frac{p}{p_s}\right) + (1-f_l)\left(\frac{p}{p_s}\right)^4 \right], \tag{5}$$

where p_s is the surface pressure and the linear term is included to reduce stratospheric relaxation times (f_l is set to 0.1). We note that although the distribution of long-wave absorbers is held fixed, water vapor is modeled prognostically by the GCM and so it influences lapse-rates independently of the structure of τ.

The insolation is constant in time (i.e., there are no seasons), and we will focus on experiments which do not include atmospheric absorption of solar radiation in order to simplify the analysis. We have repeated some experiments with the model configuration of O'Gorman and Schneider (2008b) which includes the absorption of solar radiation by the atmosphere. This is done by calculating the downward shortwave flux at a given pressure level as $S = S_0 exp(-\tau_s(p/p_s)^2)$, where $\tau_s = 0.22$ (the other model parameters are set to the same values as in O'Gorman and Schneider (2008b)). These experiments produced qualitatively similar results to our main suite of simulations (see Summary and Conclusion).

We consider four configurations of the model. The "control", Earth-like, simulation used the same parameters as listed in Table 1 of Frierson et al. (2006), with $S_{s,0}$ = 938.4 Wm^{-2}, Δ_s = 1.4, τ_{0e} = 6 and τ_{0p} = 1.5. In the uniform τ experiment the meridional gradient of τ was removed by setting

τ_0 to its average value everywhere (i.e., τ_0 = 4.5). In the uniform S_0 experiment the meridional gradient in incoming solar radiation was removed by setting Δ_s to zero, so that S_0 = 938.4 Wm^{-2} at all latitudes, while keeping the original distribution of τ_0. In a fourth experiment the gradients in τ and S_0 were both eliminated by setting both quantities to their global-mean values everywhere, which is our RCE configuration. We will refer to the latter three simulations as the "perturbation" experiments. We have also run four "global warming" experiments, in which the optical depth in each configuration is increased everywhere by 30%. Although these experiments all have the same global-mean τ, the net change in optical depth at each latitude is different in the simulations with uniform τ from the ones with meridional gradients in τ.

To estimate the radiative forcing due to these perturbations, we have repeated the perturbation experiments, but kept the SSTs fixed at their time- and zonal-mean values from the control run. The changes in the net TOA imbalance from the control simulation then define the troposphere-adjusted radiative forcings $\Delta\mathscr{F}$ (Hansen et al. 2005), shown in the top panel of Figure 1, with positive values where the downward TOA flux is increased. We note, however, that all of our runs start from the same initial conditions so these forcings are not actually applied to the GCM. In each of the perturbation experiments the forcing is negative in the tropics and positive at high latitudes, and the largest absolute value of the forcing is found at high latitudes. Setting τ uniform is the smallest perturbation, with a maximum local forcing of about 35 Wm^{-2}, while the maximum local forcing in the uniform S_0 experiment is about 168 Wm^{-2} and in the RCE simulation it is about 200Wm^{-2} (hence the forcing induced by eliminating both gradients is slightly smaller than the sum of the forcings due to eliminating each of the gradients individually). The radiative forcings in the global warming experiments are shown in the bottom panel of Figure 1.

3. Global-mean temperature

We begin by discussing how the perturbations affect the global-mean surface temperature (T_s). Before presenting the results of the simulations, we use the simplicity of the gray radiation scheme to develop some intuition for how T_s will respond to the perturbations. We consider three idealizations of the model's physics:

1. An all-troposphere atmosphere.

2. An atmosphere with a troposphere and an isothermal stratosphere.

3. An atmosphere with a troposphere and a stratosphere that is in local radiative equilibrium.

We will also assume that the tropospheric lapse-rate is only proportional to pressure.

a. All-troposphere atmosphere

For an all-troposphere atmosphere the surface temperature can be related to the OLR and τ_0 by (see Appendix A1, part a)

$$T_s(OLR, \tau_0, \gamma) = \left(\frac{OLR}{\sigma} \left(e^{-\tau_0} + \tau_0^{-\gamma} \int_0^{\tau_0} \tau'^{\gamma} e^{-\tau'} d\tau' \right)^{-1} \right)^{1/4}, \tag{6}$$

where γ is the exponent relating temperature and pressure (since we assume the lapse-rate is only proportional to pressure):

$$T = T_s \left(\frac{p}{p_s} \right)^{\gamma}.$$

The dependence of T_s on OLR, τ_0 and γ in equation 6 is shown in the left panels of Figure 2. T_s increases as these parameters are increased, though it becomes less sensitive to τ_0 when the optical depth is large, which corresponds to the runaway greenhouse regime. The global-mean S_0 (and hence the global-mean OLR) and τ_0 are fixed in the perturbation experiments, which means that in this system T_s can only change because of changes to the lapse-rate, with an increase in the lapse rate resulting in a larger surface temperature. This is essentially the lapse-rate feedback, in which an increases in the lapse-rate produces a positive feedback on the temperature response to a radiative perturbation.

b. Isothermal stratosphere

In an isothermal stratosphere the temperature is everywhere the same as the tropopause temperature T_p, which is equal to $T_s\left(\frac{\tau_p}{\tau_0}\right)^{\gamma/4}$, and equation 6 is modified to (see Appendix A1, part b)

$$T_s(OLR,\tau_0,\gamma,\tau_p)=\left(\frac{OLR}{\sigma}\left(e^{-\tau_0}+\left(\frac{\tau_p}{\tau_0}\right)^{\gamma}(1-e^{-\tau_p})+\tau_0^{-\gamma}\int_{\tau_p}^{\tau_0}\tau'^{\gamma}e^{-\tau'}d\tau'\right)^{-1}\right)^{1/4}, \qquad (7)$$

where τ_p is the optical depth at the tropopause.

The dependence of T_s on OLR, τ_0 and γ is shown in the middle columns of Figure 2. T_s now has an additional dependence on the tropopause height and the red curves in Figure 2 use $\tau_p = 0.096$, which corresponds to a tropopause height of 200hPa, while the blue curves use $\tau_p = 0.167$, which corresponds to a tropopause height of 300hPa. Both values produce curves that are very similar to the all-troposphere limit, though lowering the tropopause cools T_s for a given (OLR,τ_0,γ), and this cooling is larger for larger values of OLR, τ_0 or γ.

c. Stratosphere in radiative equilibrium

Finally, if the stratosphere is in radiative equilibrium the surface temperature is given by (see Appendix A1, part c)

$$T_s(OLR,\tau_0,\gamma,\tau_p)=\left(\frac{OLR}{\sigma}\frac{(2+\tau_p)e^{-\tau_p}/2}{e^{-\tau_0}+\tau_0^{-\gamma}\int_0^{\tau_0}\tau'^{\gamma}e^{-\tau'}d\tau'}\right)^{1/4}. \qquad (8)$$

(Robinson and Catling (2012) provided a similar derivation to the one in the appendix as part of the development of a more general analytic model for the global-mean surface temperature of planetary atmospheres in radiative-convective equilibrium (see their section 2.6)).

The new dependence of T_s on OLR, τ_0 and γ is shown in the right columns of Figure 2. T_s is warmer in this system than the all-troposphere system for small γ and colder for large γ, and lowering the tropopause now causes T_s to increase for a given (OLR, τ_0, γ), though this effect weakens for larger values of OLR, τ_0 or γ.

d. Simulation results

In the GCM the global-mean surface temperature increases by 2.4K when τ is set uniform, by 4.3K when S_0 is set uniform and by 5.7K in the RCE case (Table 1). So the warming due to eliminating both gradients simultaneously is smaller than the sum of the warmings due to eliminating the gradients individually.

Our theoretical analysis indicates that these warmings are due to increases in the lapse-rate and/or to changes in the height of the tropopause. T_s is plotted versus γ in Figure 3 (black circles, note that we take T_s to be the temperature at the lowest model level, not the SST temperature) and using the three approximations (lines). The red lines correspond to τ_p = 0.096 (i.e., a tropopause near 200hPa) and the blue lines correspond to τ_p = 0.167 (tropopause near 300hPa). For each simulation we calculate the average value of γ in the troposphere, with the tropopause defined as the height at which the lapse rate is -2Kkm^{-1}. The theoretical curves fit the data well, with the isothermal stratosphere curves matching the data slightly less well than the other two approximations. Increases in the global-mean tropospheric lapse-rate are thus the main cause of the increases in T_s, with changes in the height of the tropopause playing a secondary role.

The right panel of Figure 4 demonstrates the extent to which the tropospheric lapse-rates increase[1] in the perturbation experiments, with the largest increase (up to about -4Kkm^{-1}) in the RCE experiment and the smallest increase ($\sim$-1Kkm^{-1}) in the uniform τ experiment, matching the increases in T_s. The reasons for the increased lapse-rates are discussed in section 4c.

e. Tropopause height

The global-mean height of the tropopause (H_p) also varies in the perturbation experiments from its value of around 200hPa in the control simulation (Figure 4). In the uniform τ experiment H_p increases slightly and the transition from troposphere to stratosphere is sharper than in the control experiment (left panel of Figure 4), because the climate is more spatially homogeneous in this set-up. H_p decreases in the uniform S_0 experiment and then descends even further, to about 300hPa in the RCE experiment.

Thompson et al. (2017) recently proposed a "thermodynamic" constraint for the height of the tropopause. Starting from the thermodynamic energy equation, Thompson et al define ω_D as the cross-isentropic vertical pressure velocity required to balance diabatic heating for a given static stability

$$\omega_D = -\frac{Q}{N}, \tag{9}$$

where $N = \frac{T}{\theta}\frac{\partial\theta}{\partial p}$ is the static stability and Q is the radiative heating defined in equation 2. Under the weak-temperature gradient approximation, the dominant balance in the tropics is between diabatic heating and vertical motion acting on the static stability, so the tropopause can be defined as the height at which $\omega_D \to 0$. In the extratropics horizontal temperature advection plays a more important role in balancing diabatic heating, however horizontal temperature advection can only redistribute thermal energy and so, over a large enough domain (e.g., in the global-mean), it does

[1]We will refer to lapse-rates as "increasing" when they become more negative when using height co-ordinates.

not balance diabatic heating. In the global-mean then, the balance of equation 9 can be expected to hold to a good approximation, and constitutes a useful constraint on the global-mean tropopause height.

As discussed in the previous section, the lapse-rates increase in the perturbation experiments, and so N decreases as the troposphere becomes more unstable (middle panel of Figure 5). At the same time, Q increases in the upper tropospheres of the perturbation experiments (i.e., the radiative cooling is weaker; left panel of Figure 5). Since the global-mean optical depth profiles are the same in the four experiments, the changes in Q result from differences in the structures of the temperature profiles: as the lapse-rates increase, more of the net column radiative cooling comes from the lower troposphere. Compared with the control experiment, Q increases more in the upper tropospheres of the uniform S_0 and RCE experiments than N does, and so the tropopause descends (right panel of Figure 5). In the uniform τ experiment, however, the two effects roughly cancel and so the tropopause height is similar to the control experiment.

4. Meridional Temperature Structure

a. Emission temperature

The bottom panel of Figure 6 shows the OLR as a function of latitude for the control experiment and the three perturbation experiments. In the uniform τ case the meridional OLR gradient increases, as the tropics emit more OLR and the high latitudes emit less OLR. In the uniform S_0 case the OLR gradient reverses, as the high latitudes emit more than the tropics, demonstrating that a planet with an Earth-like distribution of long-wave absorbers but a much reduced equator-to-pole temperature gradient can emit more at high latitudes than from the tropics, a situation which might be relevant for planets with high obliquity. In the RCE case the OLR is essentially constant with latitude.

To understand these differences, consider a two box model of the atmosphere, consisting of a tropical (30°S to 30°N) box and an extratropical (everything else) box. The energy balance in each box is

$$S_1 = O_1 - F, \tag{10a}$$

$$S_2 = O_2 + F, \tag{10b}$$

where S is the insolation into the tropical box (subscript 2) or into the extratropical box (subscript 1), O is the outgoing radiation from the boxes and F is the flux of energy between the boxes, defined so that positive F corresponds to an energy transport from the tropics into the extratropics. Both S's and O's can be decomposed into a global-mean component $(\bar{\cdot})$ and a departure from that mean $(\Delta(\cdot))$:

$$S_1 = \bar{S} - \Delta S, \qquad O_1 = \bar{O} - \Delta O,$$

$$S_2 = \bar{S} + \Delta S, \qquad O_2 = \bar{O} + \Delta O.$$

Substituting into the energy balance equations and then subtracting the extratropical equation from the tropical equation

$$\Delta O = \Delta S - F. \tag{11}$$

In the uniform S_0 case ΔS is zero but the tropical box still contains more energy than the extratropical box, because of the larger optical depth in the tropics, and heat is exported from the tropics to the extratropics. So ΔO is negative in this case, and the extratropics emit more radiation than the tropics. This is analogous to what is seen in the tropical Pacific, where the warm pool region emits less OLR than the cold pool region because the higher relative humidity there makes the atmosphere optically thick in the long-wave (Pierrehumbert 1995). In the uniform τ case ΔS is unchanged from the control simulation but ΔO increases because of the reduced greenhouse effect in the tropics and the increased greenhouse effect in the extratropics. This is balanced by a reduction in the magnitude of F. Finally in the RCE case ΔS, F and ΔO are all very close to zero.

b. Surface temperature

1) Diagnostic analysis

The equator-to-pole surface temperature difference is largest in the control experiment (~54K), decreases to about 32K in the uniform τ experiment and to 15K in the uniform S_0 experiment, before going to 0 in the experiment with both gradients eliminated (Table 1). The largest temperature changes are at high latitudes, which warm by more than 40K between the control case and the case with both S_0 and τ uniform (top panel of Figure 6), while the tropics cool by about 10K. The equator-to-pole surface temperature difference in the control experiment is about 15% larger than the sum of the experiments in which a single gradient is eliminated.

We perform a local feedback analysis to diagnose the reasons for these surface temperature changes. The only radiative feedbacks in the GCM are the Planck feedback (λ_P) and the lapse-rate feedback (λ_{lr}), so we can write the local surface temperature change as (Feldl and Roe (2013); Henry and Merlis (2017)):

$$\Delta T_s(\phi) = \frac{\Delta\mathscr{F}(\phi) + \Delta[\nabla\cdot\mathbf{H}(\phi)]}{\lambda_P(\phi) + \lambda_{lr}(\phi)}, \qquad (12)$$

where $\Delta\mathscr{F}$ is the radiative forcing defined in section 2, $\mathbf{H}$ is the vertically-integrated moist static energy (MSE) flux and $\Delta T_s(\phi)$ is the zonal-mean temperature difference from the control experiment.

To estimate the Planck feedback we use the GCM's radiation scheme to calculate the difference in OLR between the equilibrated temperature field in the control simulation (T_c) and this field with 1K added at all levels and latitudes; i.e., $\lambda_P = -(OLR(T_c + 1K) - OLR(T_c))$. In other words, we calculate the radiative kernel for the Planck feedback (Soden et al. 2008). $\Delta\mathscr{F}$ is shown for the three perturbation experiments in Figure 1, and the lapse-rate feedback is calculated as a residual from equation 12, where we have calculated ΔT_s and $\Delta[\nabla \cdot \mathbf{H}(\phi)]$ directly from model output.

To understand how the different terms contribute to the total surface temperature change at each latitude, we have calculated what the surface temperature change would be if various terms were eliminated from equation 12. For instance, the magenta dashed-dot lines in Figure 7 show the temperature changes that would result if $\Delta T_s = \frac{\Delta\mathscr{F}}{\lambda_P}$; i.e., if only the Planck feedback were present. The dashed cyan lines add the meridional energy transport ($\Delta T_s = \frac{\Delta\mathscr{F}+\Delta[\nabla\cdot\mathbf{H}]}{\lambda_P}$) and the orange dotted lines show the difference between the black lines (the total surface temperature change) and the cyan lines, to indicate the effects of the lapse-rate feedback[2]. Note that a feedback is defined as positive if the sign of the forcing and of the associated temperature response are the same, and negative if the signs are different. Since the forcing is positive in the extratropics and negative in the tropics, a positive (negative) temperature change in the extratropics constitutes a positive (negative) feedback, and a negative (positive) temperature change in the tropics constitutes a positive (negative) feedback.

In the uniform τ case the Planck feedback alone underestimates the magnitude of the extratropical response (which is positive) by about half, and overestimates the magnitude of the tropical response (which is negative), also by a factor of about two (magenta line in the top panel of Figure 7). The change in the MSE flux divergence counteracts this, as less MSE is exported from the tropics to the extratropics, reducing the temperature change at all latitudes (cyan line in the top

[2] λ_{lr} changes sign at some latitudes, so $\Delta T_s = \frac{\Delta\mathscr{F}}{\lambda_{lr}}$ is not well defined.

panel of Figure 7). Finally the lapse-rate feedback is weak in the tropics, but positive and large in the extratropics, contributing a polar amplification of the response.

In the uniform S_0 case the Planck feedback alone would produce a very large temperature response, almost double the actual value of ΔT_s at all latitudes (magenta line in the middle panel of Figure 7). The MSE transport counteracts this again, substantially reducing the temperature change at all latitudes (cyan line in the middle panel of Figure 7); while the lapse-rate feedback is positive in the extratropics, increasing the temperatures there, and negative in the tropics (the magnitude of ΔT_s is reduced in the tropics). This is because the lapse-rate increases at all latitudes (see Figure 8), and so $\lambda_{lr} > 0$ at latitudes where the forcing is positive and $\lambda_{lr} < 0$ where the forcing is negative. The net effect of the lapse-rate feedback is a slight polar amplification of the temperature perturbation. The balance of terms is similar in the RCE case, but the changes are larger than in the uniform S_0 case and the lapse-rate feedback is responsible for a substantial polar amplification (bottom panel of Figure 7).

2) A PROGNOSTIC MODEL

The previous section diagnosed the causes of the zonal-mean temperature changes in the perturbation experiments. Given the simplicity of the gray radiation model, we would also like a prognostic model which can predict these changes. To do this, we again divide the atmosphere into an extratropical box (box 1) and a tropical box (box 2). Using the all-troposphere limit of section 3, and assuming again that temperature is only proportional to pressure, the surface temperature in each box can be calculated by substituting equation A2 into equation 10 and re-arranging:

$$T_1(S_1,\tau_{0,1},\gamma_1,F) = \left(\frac{S_1+F}{\sigma}\left(e^{-\tau_{0,1}} + \tau_{0,1}^{-\gamma_1}\int_0^{\tau_{0,1}} \tau'^{\gamma_1} e^{-\tau'} d\tau'\right)^{-1}\right)^{1/4}, \tag{13a}$$

$$T_2(S_2,\tau_{0,2},\gamma_2,F) = \left(\frac{S_2-F}{\sigma}\left(e^{-\tau_{0,2}} + \tau_{0,2}^{-\gamma_2}\int_0^{\tau_{0,2}} \tau'^{\gamma_2} e^{-\tau'} d\tau'\right)^{-1}\right)^{1/4}. \tag{13b}$$

This system now has five unknowns: γ_1, γ_2, F, T_1 and T_2, and so we will develop closures for the γ's and for F.

The first assumption we make is that F is proportional to the surface temperature difference $T_2 - T_1$. The top left panel of Figure 9 plots $T_2 - T_1$ and F for the eight experiments we have conducted (the control experiment, the three perturbation experiments and the four global warming experiments) and demonstrates that this is a reasonable assumption, agreeing with previous literature that has modelled meridional atmospheric energy fluxes diffusively (Sellers (1969); Kushner and Held (1998); Barry et al. (2002); Frierson et al. (2007)). So we set $F = a(T_2 - T_1)$ and estimate a by linear regression, giving a value of 2 $\mathrm{Wm^{-2}K^{-1}}$.

Next, we assume that γ_1 and γ_2 are also both proportional to $T_2 - T_1$. This assumption is based on the idea that, for a given global-mean temperature, a larger temperature difference $T_2 - T_1$ results in smaller lapse-rates throughout the troposphere (Figure 8). The top right panel of Figure 9 plots the tropical and extratropical γs in the eight simulations and again suggests that these assumptions are reasonable. So we can write equations for the two sets of γs:

$$\gamma_1 = \alpha_1(T_2 - T_1) + \beta_1, \tag{14a}$$

$$\gamma_2 = \alpha_2(T_2 - T_1) + \beta_2. \tag{14b}$$

Least-squares linear regression gives estimates for α_1, β_1, α_2 and β_2 of -0.0013$\mathrm{K^{-1}}$, 0.244, -0.0015$\mathrm{K^{-1}}$ and 0.239, respectively. We note that these values depend on the global-mean values of insolation and optical depth, and should not be taken as being universal. Furthermore, this model implies that there is a relationship between the lapse-rates and F, with $F = \frac{a}{\alpha_1}\gamma_1 - \beta_1$ (and similarly for γ_2). Since the αs are negative, this means that the meridional heat flux increases as the lapse-rates decrease.

γ_1 and γ_2 can be related as

$$\gamma_1 = \frac{\alpha_1}{\alpha_2}(\gamma_2 - \beta_2) + \beta_1 = \zeta\gamma_2 - \chi, \tag{15}$$

and so substituting into equations 13,

$$T_1(S_1, \tau_{0,1}, \gamma_2) = \left(\frac{S_1 + a(\gamma_2 - \beta_2)/\alpha_2}{\sigma} \left(e^{-\tau_{0,1}} + \tau_{0,1}^{-(\zeta\gamma_2 - \chi)} \int_0^{\tau_{0,1}} \tau'^{(\zeta\gamma_2-\chi)} e^{-\tau'} d\tau' \right)^{-1} \right)^{1/4}, \tag{16a}$$

$$T_2(S_2, \tau_{0,2}, \gamma_2) = \left(\frac{S_2 - a(\gamma_2 - \beta_2)/\alpha_2}{\sigma} \left(e^{-\tau_{0,2}} + \tau_{0,2}^{-\gamma_2} \int_0^{\tau_{0,2}} \tau_2'^{\gamma} e^{-\tau'} d\tau' \right)^{-1} \right)^{1/4}, \tag{16b}$$

and we now have a closed set of equations for γ_2. To estimate γ_2, we manipulate equation 14b such that the right hand side is zero and then find the value of γ_2 that minimizes the left hand side (note that $\gamma_2 \in \{0, 2/7\}$):

$$\begin{aligned} \gamma_2 - \alpha_2 \Bigg[& \left(\frac{S_2 - a(\gamma_2 - \beta_2)/\alpha_2}{\sigma} \left(e^{-\tau_{0,2}} + \tau_{0,2}^{-\gamma_2} \int_0^{\tau_{0,2}} \tau_2'^{\gamma} e^{-\tau'} d\tau' \right)^{-1} \right)^{1/4} \\ & - \left(\frac{S_1 + a(\gamma_2 - \beta_2)/\alpha_2}{\sigma} \left(e^{-\tau_{0,1}} + \tau_{0,1}^{-(\zeta\gamma_2 - \chi)} \int_0^{\tau_{0,1}} \tau'^{(\zeta\gamma_2-\chi)} e^{-\tau'} d\tau' \right)^{-1} \right)^{1/4} \Bigg] - \beta_2. \end{aligned} \tag{17}$$

Equation 15 can then be used to estimate γ_1, and T_1 and T_2 can be estimated from equation 16, then used to estimate F. Equivalently, one can first solve for γ_1.

The bottom left panel of Figure 9 compares estimates of T_1 and T_2 from this system with the values diagnosed from the simulations and shows that our simple model produces an excellent fit to the data from the GCM simulations. So we can predict the mean temperatures in each box (as well as the global-mean temperature) given values of S_1, S_2, τ_1 and τ_2. We have not systematically explored the ability of our model to predict temperatures across other climate states (and we note again that the parameters depend on the global-mean insolation and optical depth), but this is a promising demonstration that it has predictive power. The model is able to predict the warming of global-mean temperature in the perturbation experiments and in the global warming experiments because it includes the Planck feedback and the the lapse-rate feedback, which are the only feedbacks present in this GCM (equation 12).

Assuming a single global-mean value of γ (i.e., $\gamma_1 = \gamma_2$) for each of the simulations produces a very similar fit to the data (bottom right panel of Figure 9). This is equivalent to assuming that $\gamma_1 - \gamma_2$ is always small compared to γ, and indicates that the differences in the lapse-rate between the tropics and the extratropics are of secondary importance for the different surface temperatures and OLR values in these regions. Fixing γ at a single value for all of the simulations does not produce a good fit to the data (not shown), even though variations in γ across the simulations are of a similar magnitude to the differences between γ_1 and γ_2 (top right panel of Figure 9). This suggests that capturing the trend of γ decreasing as T_2 - T_1 increases is crucial for obtaining a good fit to the GCM data.

Given zonal-mean profiles of insolation and long-wave optical depth then, the key factors determining zonal-mean surface temperatures are the energy flux from the tropics to the extratropics and the global-mean lapse-rate.

c. Lapse-rate changes

As discussed in section 3d, the global-mean tropospheric lapse-rate increases (becomes more negative when measured in K km^{-1}) as the gradients are eliminated, with the increase being weakest in the uniform τ case and strongest in the RCE experiment (Figure 8). In the tropics this increase is easily understood because convection sets tropical temperatures in all of the experiments (Figure 10) and so the temperature profiles move to colder moist adiabats as the size of the perturbation increases.

The changes in the extratropics are more complex. The largest lapse-rates in the control case are in mid-latitudes, between about 30° and 60°, with weak lapse-rates at high latitudes ($\sim$-2K km^{-1} in the polar mid-troposphere). In the uniform τ case the high latitude lapse-rates increase significantly, and the largest lapse-rates are now near the poles. Figure 10 shows that in both these experiments the high latitudes are in "radiative-advective equilibrium" (RAE; Payne et al. (2015); Cronin and Jansen (2016)), with horizontal energy fluxes balancing radiative cooling. The high latitude lapse-rates increase further in the uniform S_0 case, and these regions also transition to being in radiative-convective equilibrium, and then the lapse-rates decrease slightly in the RCE case.

We use a one-level energy balance model to understand this behavior (Abbot and Tziperman (2009); Payne et al. (2015)). This consists of a surface level with temperature T_s and an atmospheric level with temperature T_a. In equilibrium the energy balances for the surface and the atmosphere are, respectively,

$$0 = \varepsilon\sigma T_a^4 - \sigma T_s^4 + F_s - F_c, \qquad \text{(surface)} \tag{18a}$$

$$0 = \varepsilon\sigma T_s^4 - 2\varepsilon\sigma T_a^4 + F_a + F_c, \qquad \text{(atmosphere)} \tag{18b}$$

where F_s is the solar flux absorbed at the surface, F_a is the meridional advective heat flux by the atmosphere, F_c is the vertical convective heat flux and $\varepsilon = 1 - e^{-\tau_0}$ is the atmospheric emissivity (and hence absorptivity).

For a system in RAE, in which $F_c \sim 0$, this system can be solved for T_s and T_a to give

$$T_s = \left[\frac{2F_s + F_a}{\sigma(2-\varepsilon)}\right]^{1/4}, \tag{19a}$$

$$T_a = \left[\frac{\varepsilon F_s + F_a}{\sigma\varepsilon(2-\varepsilon)}\right]^{1/4}. \tag{19b}$$

The left panel of Figure 11 plots how the temperature difference $T_s - T_a$ varies in RAE as a function of F_a and ε for $F_s = 97.6\mathrm{Wm}^{-2}$, the mean insolation averaged over latitudes polewards of 60° of in the control and uniform τ simulations. The temperature difference increases as the optical depth increases, and decreases when the meridional energy flux increases.

The round markers on this panel indicate the values of ε and F_a from the control and uniform τ_0 experiments, where both these quantities are also averaged over latitudes polewards of 60° and we take F_a to be the vertically-integrated meridional heat flux. This suggests that $T_s - T_a$ will increase from about 20K to about 26K, whereas in the GCM $T_s - T_a$ increases from 16K to 28K (we take 600hPa as the representative atmospheric level). While the temperature difference should not be taken as a direct measure of the lapse-rate, as the representative atmospheric level can vary, this demonstrates that the increase in the high latitude lapse-rates in the uniform τ_0 experiment is primarily caused by the increased optical depths there, with the slight reduction in F_a playing a secondary role. Figure 2 of Cronin and Jansen (2016) also demonstrates how lapse-rates increase in RAE atmospheres as the optical depth increases.

That these cases are in RAE means that they are stable to convection, hence we would expect the lapse-rates to be higher in the uniform S_0 and RCE cases, because the high latitudes of these simulations are convecting (Figure 10). But the high latitude insolation also increases in these experiments, so we cannot infer this directly and instead must compare how the convecting lapse-rates in these experiments compare with the RAE lapse-rates in the experiments with weaker high latitude insolation.

The right panel of Figure 11 plots the critical temperature difference above which the model is unstable to convection for $S_0 = 234.6\text{Wm}^{-2}$ (assuming $F_a = 0$). To calculate this curve we assume that the moist static energy at the surface is equal to the moist static energy at the representative atmospheric level:

$$c_p T_s + L_v r_s = c_p T_a + L_v r_a^* + g z_a, \tag{20}$$

where L_v is the latent heat of evaporation, r_s is the surface specific humidity, r_a^* is the saturation specific humidity at the atmospheric level and z_a is the height of the atmospheric level. Following Abbot and Tziperman (2009), we use a surface relative humidity of 80% and calculate z_a using a scale height of 8km. T_a, T_s and F_c can be solved for by combining this equation with the one-layer model, after specifying F_s. (The round markers show the RAE temperature differences for the uniform S_0 and RCE cases, assuming F_a = 100 Wm^{-2}).

Comparing with the left panel confirms that the critical temperature difference in the uniform S_0 and RCE cases is larger than the (RAE) temperature differences in the control and uniform τ cases. Hence the lapse-rates increase in the uniform S_0 and RCE cases compared to the control and uniform τ experiments because the increased insolation makes the high latitudes unstable to moist convection, as evidenced by the two round markers in the right panel of Figure 11 lying above the curve of critical temperatures. This causes a transition from RAE to RCE, and the critical lapse-rates for this insolation value (234.6 Wm^{-2}) are larger than the RAE lapse-rates in the presence of the weaker insolation (97.6 Wm^{-2}). The right panel of Figure 11 also shows that the critical temperature difference decreases as the optical depth increases (see also Figure 1 of Abbot and Tziperman (2009)), explaining why the high latitude lapse-rates are larger in the uniform S_0 case than in the RCE case.

5. Temperature Response to Forcings

As mentioned in section 2, we also performed experiments with each of the four configurations in which τ was increased by 30%, which mimics the effects of increased CO_2 concentrations in this GCM. We note again that although the global-mean change in τ is the same in all of the configurations, in the control set-up the forcing is larger in the tropics than in the extratropics, whereas the forcings in the perturbation set-ups are homogeneous in latitude (bottom panel of Figure 1).

Interestingly, the global-mean temperature change is insensitive to the base state, as in all four cases T_s increases by between 4 and 4.2K (Table 1). There are substantial differences in the latitudinal structure of this warming, however (top left panel of Figure 12), and the similar sensitivities in the four configurations may be a coincidence. Most importantly, in the control case there is a polar amplification of about 6K, in the uniform τ case the polar amplification is about 3.7K, in the uniform S_0 case the polar amplification is about 1K, and there is no amplification in the RCE case.

The other panels in Figure 12 explore the reasons for these responses, using the diagnostic framework of equation 12. The top right panel shows that the forcing and Planck feedback alone result in a tropically-amplified warming in the the control set-up (black curve). The forcing decreases away from the equator (bottom panel of Figure 1), as does the magnitude of the Planck feedback parameter (not shown). Close to the tropics these changes cancel out so that $\Delta\mathscr{F}/\lambda_P$ is relatively uniform, but at higher latitudes the forcing decreases faster than the Planck feedback and $\Delta\mathscr{F}/\lambda_P$ decreases (see section 2 of Henry and Merlis (2017) for a discussion of these patterns). This is countered by the changes in the horizontal energy flux (bottom left panel) and, to a lesser extent, by the lapse-rate feedback, which is negative in the tropics and positive at higher latitudes (bottom right panel).

The reason for the positive lapse-rate feedback at high latitudes can be seen from the left panel of Figure 11: increasing the optical depth increases the lapse-rate in RAE, though this is countered somewhat by the increased meridional heat flux. We refer the reader to Payne et al. (2015), Cronin and Jansen (2016) and Henry and Merlis (2017) for more in-depth investigations of why the lapse-rate feedback is positive at high latitudes and negative at low latitudes for Earth-like gray-radiation models. Pithan and Mauristen (2014) also found a strong polar amplification of warming due to the lapse-rate feedback in an analysis of CMIP5 models.

In the uniform τ set-up the forcing is approximately constant in latitude and so $\Delta\mathscr{F}/\lambda_P$ contributes a polar amplification of about 1.5K, because the Plank feedback decreases away from the equator. The bulk of the polar amplification still comes from the change in MSE transport, while the lapse-rate feedback is roughly constant in latitude and negative. This means that the lapse-rate decreases uniformly in the global-warming simulation, including at high latitudes. The reason for the reduced high latitude lapse-rates can be seen from the differences between the red crosses and the black circles in Figure 11: because the emissivity is already so high in the high latitudes of this experiment, increasing it further does not impact the lapse-rate substantially and so the lapse-rate is mainly reduced by the increased meridional heat flux.

In the uniform S_0 set-up $\Delta\mathscr{F}/\lambda_P$ has little meridional structure and the polar amplification comes entirely from the changes in the meridional heat transport. The lapse-rate feedback is negative and roughly uniform in latitude, as all latitudes are in RCE. That the polar amplification in the control set-up, the uniform τ set-up and the uniform S_0 set-up are all mainly due to meridional heat transport agrees with the results from our prognostic model, which suggest that meridional variations of the lapse-rate feedback are of secondary importance for capturing the polar amplification of warming in the GCM. Finally, in the RCE case all the changes are homogeneous in latitude.

The strongly negative lapse-rate feedbacks in the perturbation set-ups are responsible for the fact that the global-mean surface temperature changes are roughly the same in all four configurations despite the global-mean forcings being substantially larger in the perturbation set-ups than in the control set-up (bottom panel of Figure 1).

6. Summary and Conclusion

In this study we have investigated the response of a moist, idealized GCM to eliminating the meridional gradients in insolation and in long-wave optical depth. We have performed experiments in which these gradients were eliminated separately (the uniform τ and uniform S_0 experiments), and an experiment in which both were eliminated at the same time (the RCE experiment); and have used a number of simple models to interpret the differences in the climates of the model configurations.

Our first main result is that eliminating these gradients causes the global-mean surface temperature of the model to increase. A one-dimensional system consisting of an all-troposphere atmosphere with temperature proportional to pressure captures the temperature changes across these simulations, demonstrating that the increased lapse-rates in the perturbation experiments are primarily responsible for the increased surface temperatures. The lapse-rates increase at all latitudes in the perturbation experiments, but for a variety of reasons. In the tropics, the lapse-rates increase because the tropics cool and so tropospheric temperatures move to colder moist adiabats. In the uniform τ experiment the extratropical lapse-rates increase because of the increased high latitude optical depths, while in the uniform S_0 and RCE experiments the extratropical lapse-rates increase because of the increased high latitude insolation, which de-stabilizes the high latitudes and causes a transition from RAE to RCE there (see Abbot and Tziperman (2008) for a discussion of high latitude convection and its implications for equable climates).

In the global-mean, the tropopause descends in the uniform S_0 and RCE experiments, but is slightly higher in the uniform τ experiment. We have used the thermodynamic constraint of Thompson et al. (2017) to explain these variations. In the uniform S_0 and RCE experiments the tropopause descends because the radiative heating profile becomes more bottom-heavy and goes to zero lower in the atmosphere compared to the control simulation. The radiative heating profile also becomes more bottom-heavy in the uniform τ experiment, but this is over-compensated for by the reduced tropospheric stability and so the tropopause rises slightly.

Moving on to regional changes, the OLR increases in the tropics and decreases in the extratropics in the uniform τ experiment compared with the control. In the uniform S_0 experiment the OLR is largest at high latitudes, which is similar to the present-day Earth's tropics, where regions of colder SSTs emit more radiation to space because of the optically-thinner overlying atmosphere. The OLR is constant with latitude in the RCE experiment.

A linear feedback analysis shows that the Planck feedback causes a strong polar amplification of the response in all of the perturbation experiments, when compared to the control. This is damped somewhat by a reduction in the meridional moist static energy flux, while the lapse-rate feedbacks are large and positive in the extratropics and weakly positive in the tropics, contributing to the polar amplification of the responses. Complementing this diagnostic analysis, we have also presented a prognostic model of zonal surface temperatures in this GCM, which accurately predicts the tropical and extratropical temperatures across the eight simulations (the control simulation, the three perturbation experiments and the four global warming experiments). The success of this model demonstrates that, given zonal-mean profiles of insolation and long-wave optical depth, the energy flux from the tropics to the extratropics and the global-mean lapse-rate are the main factors controlling zonal-mean surface temperatures. Similar box models for the temperature structures of tidally-locked, rocky planets have been developed by Yang and Abbot (2014) and Koll and Abbot (2016), and provide some suggestions for how clouds could be added to our model.

To summarize these results, relative to the RCE case, adding the meridional gradient in long-wave optical depth (the uniform S_0 case) produces a climate that is analogous to what is seen in the tropical Pacific, with the warmer tropics playing the role of the west Pacific and emitting less radiation than the cooler extra-tropics (the east Pacific) (Pierrehumbert 1995). Adding the insolation gradient without adding the optical depth gradient produces a climate that is similar to the control climate, but has weaker horizontal energy transports and more convection outside the tropics. As might be expected then, the insolation gradient has a larger influence on the model's climate than the gradient in optical depth, though both make sizeable contributions to the equator-to-pole temperature gradient and to the GCM's climate in general.

The global-mean surface temperature response to increasing the optical depth by 30% is the same in all four configurations, however the effective forcing is significantly larger in the perturbation set-ups than in the control set-up, and this is countered by the stronger lapse-rate feedback in these experiments. In the control set-up the forcing and Planck feedback alone would lead to a tropical amplification of the warming, while these produce a polar amplification of the warming in the uniform τ set-up. In all but the RCE case, the changes in MSE flux act to polar amplify the warming, and in the control configuration the lapse-rate feedback also contributes to the polar amplification. In the other experiments the lapse-rate feedback is negative at all latitudes, with little meridional structure.

Our study is an important first step for understanding the roles the meridional gradients of insolation and long-wave optical depth play in setting up Earth's climate, and future studies with comprehensive models will be able to build off the insights obtained here. The experiments with solar absorption by the atmosphere included gave qualitatively similar results to our main suite of experiments, though the quantitative agreement with our theoretical models is not as good (the magenta squares and line in Figure 3 are an example). It is also worth noting that the co-efficient of short-wave absorption is fixed in latitude and height in these experiments (see section 2), and so it does not include the effects of latitudinal variations in atmospheric water vapor (or ozone) concentrations.

This leaves clouds and the water vapor feedback as the main atmospheric processes still to be accounted for, as well as the dynamics of ice sheets, the ocean and land surface processes (Winton (2003) explored the climate response to eliminating meridional ocean heat transport in two coupled climate models). Our model also did not include a seasonal cycle, which would affect the mean climate states of our different configurations. For instance, winter inversions could develop at the high latitudes of planets whose insolation is globally uniform in the annual-mean, insulating the surface climate there from the overlying atmosphere and inhibiting high latitude convection. In a model capable of simulating low level stratocumulus clouds this would likely cause a substantial cooling of high latitude surface temperatures (Abbot 2014).

Comparing simulations with more comprehensive models to our idealized GCM results will allow the effects of these different factors to be isolated, while the simple conceptual models we have developed and used here provide a useful framework for developing a complete understanding of how Earth's climate would be affected by eliminating the gradients in insolation and/or in long-wave optical depth.

APPENDIX

A1. Derivations of Equations 6, 7 and 8

a. All-troposphere atmosphere

Equation 1a can be solved at $\tau = 0$ to give

$$OLR(T,\tau_0) = U(\tau_0)e^{-\tau_0} + \int_0^{\tau_0} \sigma T(\tau')^4 e^{-\tau'} d\tau'. \tag{A1}$$

If the lapse-rate is only proportional to pressure then

$$T = T_s \left(\frac{p}{p_s}\right)^{\gamma},$$

where $\gamma = R/c_p = 2/7$ for a dry atmosphere and $\gamma < 2/7$ for a moist atmosphere. Since $\tau/\tau_0 \approx (p/p_s)^4$

$$T \approx T_s \left(\frac{\tau}{\tau_0}\right)^{\gamma/4}.$$

Substituting into equation A1 gives

$$\begin{aligned} OLR(T_s, \tau_0, \gamma) &= \sigma T_s^4 e^{-\tau_0} + \int_0^{\tau_0} \sigma T_s^4 \left(\frac{\tau'}{\tau_0}\right)^{\gamma} e^{-\tau'} d\tau', \\ &= \sigma T_s^4 \left(e^{-\tau_0} + \tau_0^{-\gamma} \int_0^{\tau_0} \tau'^{\gamma} e^{-\tau'} d\tau'\right), \end{aligned} \tag{A2}$$

which can be rearranged for T_s:

$$T_s(OLR, \tau_0, \gamma) = \left(\frac{OLR}{\sigma}\left(e^{-\tau_0} + \tau_0^{-\gamma}\int_0^{\tau_0} \tau'^{\gamma} e^{-\tau'} d\tau'\right)^{-1}\right)^{1/4}. \tag{A3}$$

Note that if $\tau_0 \to \infty$ then the integral is the Γ-function with argument $\gamma + 1$

$$T_s(OLR, \tau_0, \gamma) = \left(\frac{OLR}{\sigma}\left(e^{-\tau_0} + \tau_0^{-\gamma}\Gamma(\gamma+1)\right)^{-1}\right)^{1/4}.$$

(see section 4.3.2 of Pierrehumbert (2011)).

b. Isothermal stratosphere

For an atmosphere with an isothermal stratosphere above the troposphere equation A1 can be written as

$$OLR(T, \tau_0, \tau_p) = U(\tau_0) e^{-\tau_0} + \int_0^{\tau_p} \sigma T(\tau')^4 e^{-\tau'} d\tau' + \int_{\tau_p}^{\tau_0} \sigma T(\tau')^4 e^{-\tau'} d\tau', \tag{A4}$$

where τ_p is the optical depth at the tropopause. Using the results of the previous subsection,

$$OLR(T, \tau_0, \gamma, \tau_p) = \sigma T_s^4 \left(e^{-\tau_0} + \tau_0^{-\gamma}\int_{\tau_p}^{\tau_0} \tau'^{\gamma} e^{-\tau'} d\tau'\right) + \int_0^{\tau_p} \sigma T(\tau')^4 e^{-\tau'} d\tau'.$$

The temperature of the stratosphere is everywhere the same as the tropopause temperature T_p, which is equal to $T_s \left(\frac{\tau_p}{\tau_0}\right)^{\gamma/4}$ and so the second integral can be evaluated to give

$$OLR(T_s, \tau_0, \gamma, \tau_p) = \sigma T_s^4 \left(e^{-\tau_0} + \left(\frac{\tau_p}{\tau_0}\right)^{\gamma}(1 - e^{-\tau_p}) + \tau_0^{-\gamma}\int_{\tau_p}^{\tau_0} \tau'^{\gamma} e^{-\tau'} d\tau'\right), \tag{A5}$$

and the surface temperature is

$$T_s(OLR,\tau_0,\gamma,\tau_p) = \left(\frac{OLR}{\sigma}\left(e^{-\tau_0} + \left(\frac{\tau_p}{\tau_0}\right)^{\gamma}(1-e^{-\tau_p}) + \tau_0^{-\gamma}\int_{\tau_p}^{\tau_0}\tau'^{\gamma}e^{-\tau'}d\tau'\right)^{-1}\right)^{1/4}. \quad \text{(A6)}$$

If $\tau_p = 0$ then we return to equation 6 of the all-troposphere limit.

c. Stratosphere in radiative equilibrium

Radiative equilibrium demands that the net divergence of the radiative flux be zero everywhere such that the net heating by the radiation vanishes

$$\frac{d}{d\tau}(U(\tau) - D(\tau)) = U + D - 2\sigma T^4 = 0, \quad \text{(A7)}$$

and hence $U - D$ is constant. Using the boundary conditions at $\tau = 0$, $U - D = OLR$ and so adding equations 1a and 1b,

$$\frac{d}{d\tau}(U(\tau) + D(\tau)) = U - D = OLR,$$

and then integrating

$$U(\tau) + D(\tau) = OLR(1+\tau).$$

Substituting from equation A7 results in an equation for the stratospheric temperature in radiative equilibrium

$$2\sigma T^4 = OLR(1+\tau). \quad \text{(A8)}$$

Substituting into equation A4 and re-arranging then gives

$$OLR(T_s,\tau_0,\gamma,\tau_p) = \frac{e^{-\tau_0} + \tau_0^{-\gamma}\int_0^{\tau_0}\tau'^{\gamma}e^{-\tau'}d\tau'}{(2+\tau_p)e^{-\tau_p}/2}\sigma T_s^4, \quad \text{(A9)}$$

and so

$$T_s(OLR,\tau_0,\gamma,\tau_p) = \left(\frac{OLR}{\sigma}\frac{(2+\tau_p)e^{-\tau_p}/2}{e^{-\tau_0} + \tau_0^{-\gamma}\int_0^{\tau_0}\tau'^{\gamma}e^{-\tau'}d\tau'}\right)^{1/4}. \quad \text{(A10)}$$

Acknowledgment. We thank Daniel Koll, Levi Silvers and Tim Cronin for helpful discussions and for comments on earlier versions of this manuscript. We also thank Dorian Abbot, Nadir Jeevanjee and an anonymous reviewer for thorough readings of the manuscript and productive comments.

References

Abbot, D. S., 2014: Resolved snowball earth clouds. *Journal of Climate*, **27 (630)**, 4391–4402.

Abbot, D. S., and E. Tziperman, 2008: A high-latitude convective cloud feedback and equable climates. *Quarterly Journal of the Royal Meteorological Society*, **134 (630)**, 165–185.

Abbot, D. S., and E. Tziperman, 2009: Controls on the activation and strength of a high-latitude convective cloud feedback. *Journal of the Atmospheric Sciences*, **66 (630)**, 519–529.

Arnold, N. P., and D. A. Randall, 2015: Global-scale convective aggregation: Implications for the madden-julian oscillation. *Journal of Advances in Modeling Earth Systems*, **7 (4)**, 1499–1518.

Arnold, N. P., E. Tziperman, and B. Farrell, 2010: Abrupt transition to strong superrotation driven by equatorial wave resonance in an idealized gcm. *Journal of the Atmospheric Sciences*, **69**, 626–640.

Barry, L., G. C. Craig, and J. Thuburn, 2002: Poleward heat transport by the atmospheric heat engine. *Nature*, **415 (22)**, 774–777.

Bischoff, T., and T. Schneider, 2016: The equatorial energy balance, itcz position, and double itcz bifurcations. *Journal of Climate*, **29 (15)**, 2997–3013.

Caballero, R., and M. Huber, 2014: State-dependent climate sensitivity in past warm climates and its implications for future climate projections. *Proceedings of the National Academy of Sciences*, **110 (35)**, 14 162–14 167.

Chao, W. C., and B. Chen, 2004: Single and double itcz in an aqua-planet model with constant sea surface temperature and solar angle. *Climate Dynamics*, **22 (15)**, 447–459.

Coppin, D., and S. Bony, 2015: Physical mechanisms controlling the initiation of convective self-aggregation in a general circulation model. *Journal of Advances in Modeling Earth Systems*, **7 (4)**, 2060–2078.

Coppin, D., and S. Bony, 2017: Internal variability in a coupled general circulation model in radiative-convective equilibrium. *Geophysical Research Letters*, **44 (10)**, 5142–5149.

Cronin, T. W., and M. F. Jansen, 2016: Analytic radiative-advective equilibrium as a model for high-latitude climate. *Geophysical Research Letters*, **43 (15)**, 449–457.

Feldl, N., and G. H. Roe, 2013: Four perspectives on climate feedbacks. *Geophysical Research Letters*, **40 (15)**, 4007–4011.

Frierson, D. M. W., 2007: The dynamics of idealized convection schemes and their effect on the zonally averaged tropical circulation. *Journal of the Atmospheric Sciences*, **64 (23)**, 1959–1976.

Frierson, D. M. W., I. M. Held, and P. Zurita-Gotor, 2006: A gray-radiation aquaplanet moist gcm. part i: Static stability and eddy scales. *Journal of the Atmospheric Sciences*, **63 (23)**, 2548–2566.

Frierson, D. M. W., I. M. Held, and P. Zurita-Gotor, 2007: A gray-radiation aquaplanet moist gcm. part ii: Energy transports in altered climates. *Journal of the Atmospheric Sciences*, **64 (23)**, 1680–1693.

Hansen, J., and Coauthors, 2005: Efficacy of climate forcings. *Journal of Geophysical Research: Atmospheres*, **110 (D18)**, d18104.

Held, I. M., 2000: The general circulation of the atmosphere *Woods Hole Lecture Notes*. URL http://www.gfdl.noaa.gov/cms-filesystem-action/userfiles/ih/lectures/woodshole.pdf.

Henry, M., and T. M. Merlis, 2017: The role of the nonlinearity of the stefan-boltzmann law on the structure of radiatively forced temperature change. *Journal of Climate*, Submitted.

Huber, M., and L. C. Sloan, 2001: Heat transport, deep waters, and thermal gradients: Coupled simulation of an eocene greenhouse climate. *Geophysical Research Letters*, **28 (18)**, 3481–3484.

Kirtman, B. P., and E. K. Schneider, 2000: A spontaneously generated tropical atmospheric general circulation. *Journal of the Atmospheric Sciences*, **57 (7)**, 2080–2093.

Koll, D. D., and D. S. Abbot, 2016: Temperature structure and atmospheric circulation of dry tidally locked rocky exoplanets. *The Astrophysical Journal*, **825 (2)**, 1–21.

Kushner, P. J., and I. M. Held, 1998: A test, using atmospheric data, of a method for estimating ocean eddy diffusivity. *Geophysical Research Letters*, **25 (22)**, 4213–4216.

Levine, X. J., and T. Schneider, 2015: Baroclinic eddies and the extent of the hadley circulation: An idealized gcm study. *Journal of the Atmospheric Sciences*, **72 (15)**, 2744–2761.

Lutsko, N. J., 2017: The response of an idealized atmosphere to localized tropical heating: Superrotation and the breakdown of linear theory. *Journal of the Atmospheric Sciences*, In press.

Merlis, T. M., W. Zhou, I. M. Held, and M. Zhao, 2016: Surface temperature dependence of tropical cyclone-permitting simulations in a spherical model with uniform thermal forcing. *Geophysical Research Letters*, **43 (6)**, 2859–2865.

O'Gorman, P. A., and T. Schneider, 2008a: Energy of midlatitude transient eddies in idealized simulations of changed climates. *Journal of Climate*, **21 (15)**, 5797–5806.

O'Gorman, P. A., and T. Schneider, 2008b: The hydrological cycle over a wide range of climates simulated with an idealized gcm. *Journal of Climate*, **21 (15)**, 3815–3832.

Payne, A. E., M. F. Jansen, and T. W. Cronin, 2015: Conceptual model analysis of the influence of temperature feedbacks on polar amplification. *Geophysical Research Letters*, **42 (15)**, 9561–9570.

Pendergrass, A. G., K. A. Reed, and B. Medeiros, 2016: The link between extreme precipitation and convective organization in a warming climate: Global radiative-convective equilibrium simulations. *Geophysical Research Letters*, **43 (21)**, 11,445–11,452.

Pierrehumbert, R., 1995: Thermostats, radiator fins, and the local run-away greenhouse. *Journal of the Atmospheric Sciences*, **52 (23)**, 1784–1806.

Pierrehumbert, R., 2011: *Principles of Planetary Climate*. Cambridge University Press.

Pierrehumbert, R. T., 2005: Climate dynamics of a hard snowball earth. *Journal of Geophysical Research: Atmospheres*, **110 (D1)**.

Pithan, F., and T. Mauristen, 2014: Arctic amplification dominated by temperature feedbacks in contemporary climate models. *Nature Geoscience*, **7 (15)**, 181–184.

Popke, D., B. Stevens, and A. Voigt, 2013: Climate and climate change in a radiative-convective equilibrium version of echam6. *Journal of Advances in Modeling Earth Systems*, **5 (1)**, 1–14.

Popp, M., H. Schmidt, and J. Marotzke, 2016: Transition to a moist greenhouse with co2 and solar forcing. *Nature Communications*, **7 (10627)**.

Reed, K. A., B. Medeiros, J. T. Bacmeister, and P. H. Lauritzen, 2015: Global radiativeconvective equilibrium in the community atmosphere model, version 5. *Journal of the Atmospheric Sciences*, **72 (15)**, 2183–2187.

Robinson, T. D., and D. C. Catling, 2012: An analytic radiative-convective model for planetary atmospheres. *The Astrophysical Journal*, **757 (104)**, 1–12.

Schneider, T., P. A. O'Gorman, and X. J. Levine, 2010: Water vapor and the dynamics of climate changes. *Reviews of Geophysics*, **48 (3)**.

Schneider, T., and C. C. Walker, 2006: Self-organization of atmospheric macroturbulence into critical states of weak nonlinear eddyeddy interactions. *Journal of the Atmospheric Sciences*, **63 (15)**, 1569–1586.

Sellers, W. D., 1969: A climate model based on the energy balance of the earth-atmosphere system. *Journal of Applied Meteorology*, **8 (22)**, 392–400.

Shi, X., and C. S. Bretherton, 2014: Large-scale character of an atmosphere in rotating radiative-convective equilibrium. *Journal of Advances in Modeling Earth Systems*, **6 (3)**, 616–629.

Soden, B. J., I. M. Held, R. Colman, K. M. Shell, J. T. Kiehl, and C. A. Shields, 2008: Quantifying climate feedbacks using radiative kernels. *Journal of Climate*, **21 (7)**, 3504–3520.

Sumi, A., 1992: Pattern formation of convective activity over the aqua-planet with globally uniform sea surface temperature. *Journal of the Meteorological Society of Japan*, **70 (15)**, 855–876.

Thompson, D. W. J., S. Bony, and Y. Li, 2017: Thermodynamic constraint on the depth of the global tropospheric circulation. *Proceedings of the National Academy of Sciences*, **114 (41)**, 8181–8186.

TABLE 1. List of model configurations, with corresponding values of global-mean surface temperature and equator-to-pole temperature difference in the control and perturbation experiments, as well as the global-mean surface temperature response to increasing τ everywhere by 30%.

Configuration	Global-mean surface temperature (GMST) [K]	Equator-to-pole surface temperature difference [K]	GMST response to $\tau \times 1.3$ [K]
control	280.5	54.2	4.1
uniform τ	282.9	31.8	4.2
uniform S_0	284.8	15.3	4.0
both uniform	286.2	0.03	4.1

Vallis, G. K., 2006: *Atmospheric and Oceanic Fluid Dynamics*. 1st ed., Cambridge University Press, Cambridge, UK.

Winton, M., 2003: On the climatic impact of ocean circulation. *Journal of Climate*, **21 (6)**, 2875–2889.

Yang, J., and D. S. Abbot, 2014: A low-order model of water vapor, clouds, and thermal emission for tidally locked terrestrial planets. *The Astrophysical Journal*, **784 (155)**, 1–12.

Zurita-Gotor, P., and G. K. Vallis, 2011: Dynamics of midlatitude tropopause height in an idealized model. *Journal of the Atmospheric Sciences*, **68 (15)**, 823–838.

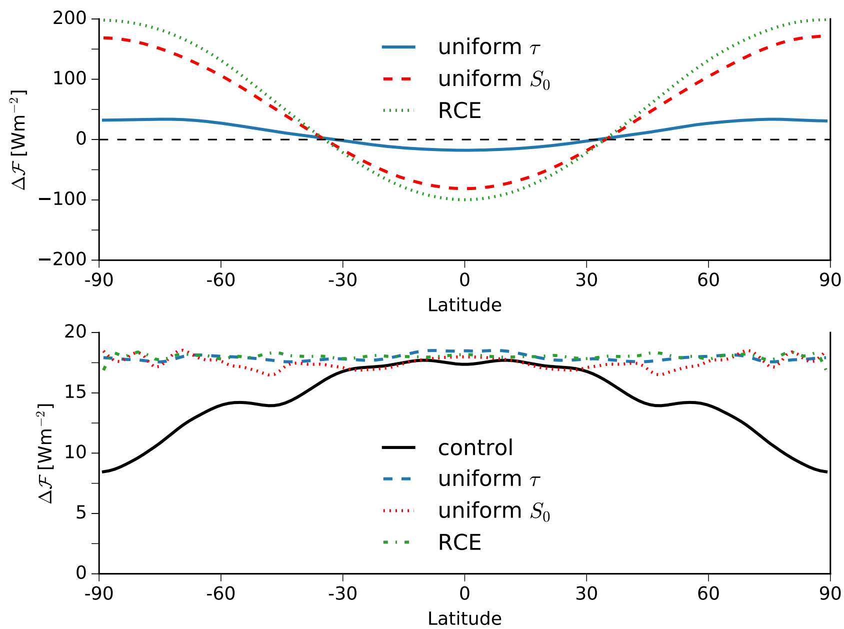

FIG. 1. Top panel: Troposphere and stratosphere-adjusted radiative forcing $\Delta\mathscr{F}$ for the three perturbation experiments (see text for description of how $\Delta\mathscr{F}$ is calculated). The global-mean forcings are 1.87Wm^{-2}, 2.26Wm^{-2} and 2.71Wm^{-2} for the uniform τ, uniform S_0 and RCE cases, respectively. Bottom panel: Troposphere and stratosphere-adjusted radiative forcing $\Delta\mathscr{F}$ for the four global warming experiments. The forcing is positive where the downward flux at TOA is increased. The global-mean forcings are 15.74Wm^{-2}, 17.97Wm^{-2}, 17.40Wm^{-2} and 18.02Wm^{-2} for the control, uniform τ, uniform S_0 and RCE configurations, respectively.

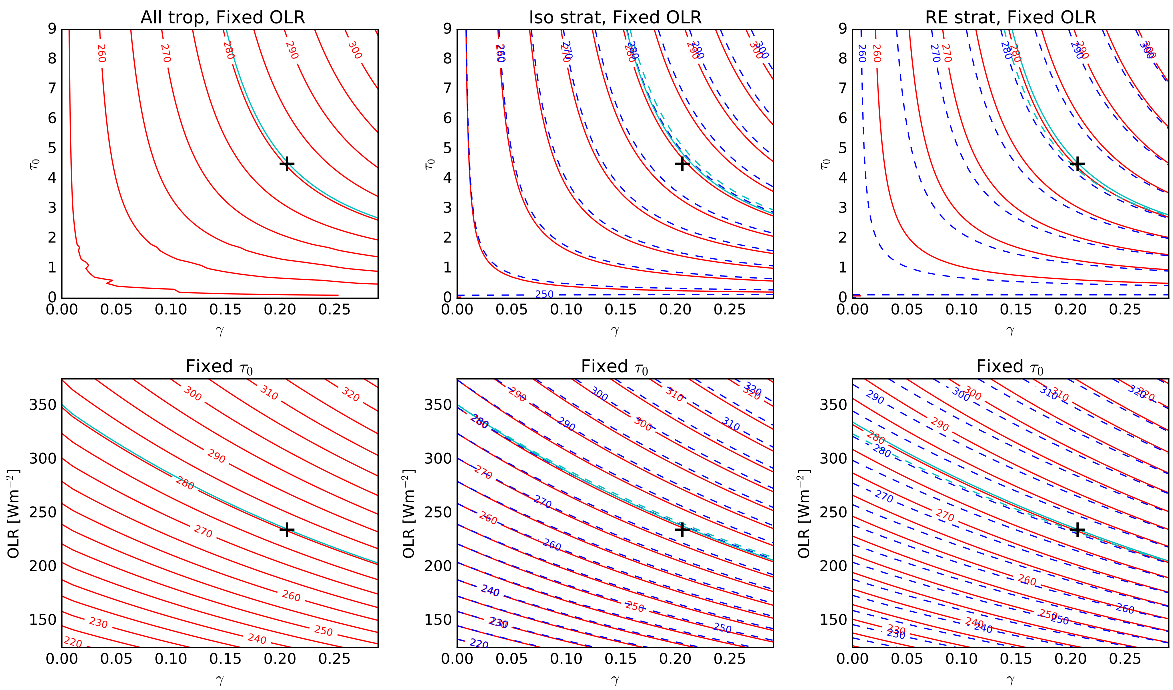

FIG. 2. Contour plots of T_s as a function of τ_0 and γ (top panels) and as a function of *OLR* and γ (bottom panels), for the all troposphere atmosphere (left panel), the atmosphere with isothermal stratosphere (middle panel) and the atmosphere with radiative-equilibrium stratosphere (right panel). The black crosses mark the values of τ_0 (top panels) or *OLR* (bottom panels) and γ in the control simulation. In the top panels $OLR = 234.6$ Wm^{-2} and in the bottom panels $\tau_0 = 4.5$. In the second and third columns the red curves are calculated with τ_p = 0.0965, which is equivalent to a tropopause height of 200hPa and the dashed blue lines are calculated with τ_p = 0.167, which is equivalent to a tropopause height of 300hPa. The cyan lines show the 280.5K contour, which is the surface temperature in the control simulation (solid lines use $\tau_p = 0.0965$ and dashed lines use $\tau_p = 0.167$).

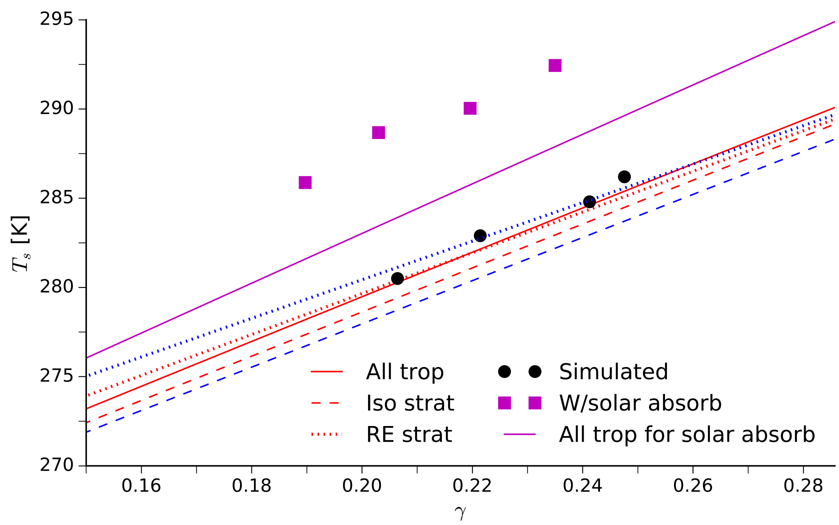

FIG. 3. T_s versus γ for the control simulation and the three perturbation simulations (dots) and the theoretical relationships from equations 6 (solid), 7 (dashed) and 8 (dotted). The red curves use τ_p = 0.096 and the blue curves use τ_p = 0.167. γ is calculated in the simulations as the average value of γ in the troposphere, with the tropopause defined as the height at which the lapse rate is -2Kkm^{-1}. The magenta squares show the results for simulation which include solar absorption by the atmosphere and the magenta line shows the curve for equation 6 using the global-mean OLR and τ_0 values from the experiments with solar absorption included.

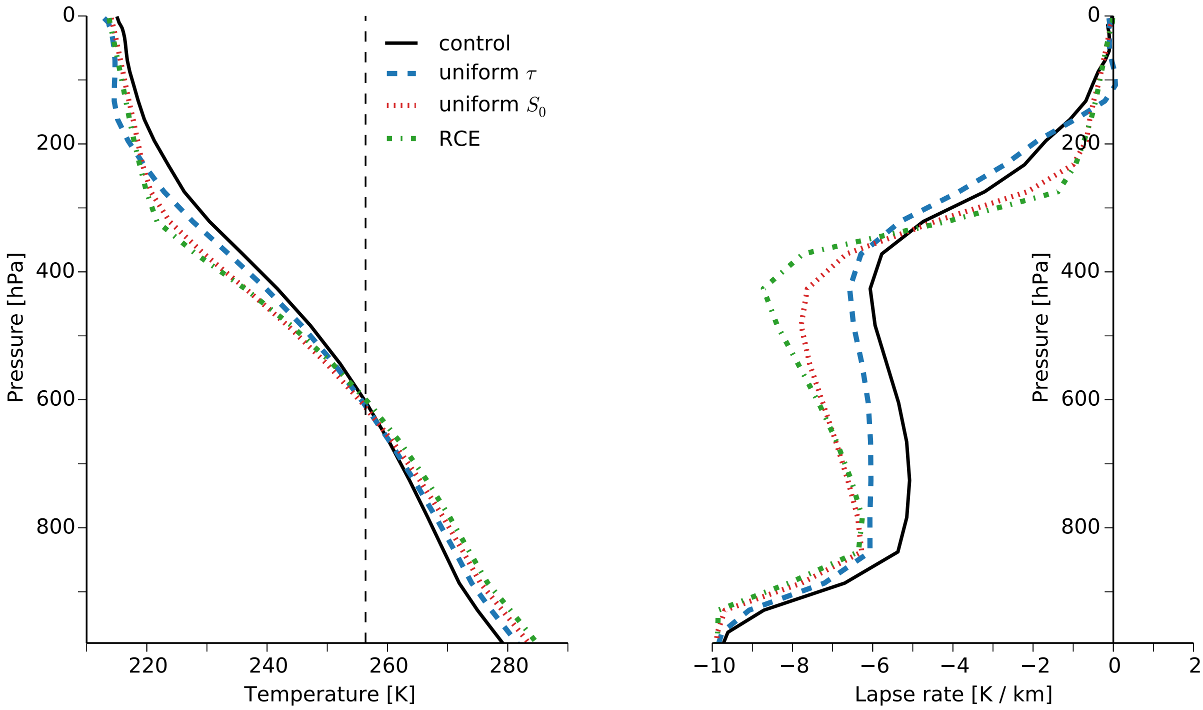

FIG. 4. Left panel: global-mean temperature profiles for the control experiment and the three perturbation experiments. The black dashed line shows the emission temperature $T_E = (S_{s,0}/4\sigma)^{1/4}$. Right panel: global-mean lapse-rate profiles for the same experiments. The tropopause is defined as the altitude at which the lapse rate is -2Kkm^{-1}.

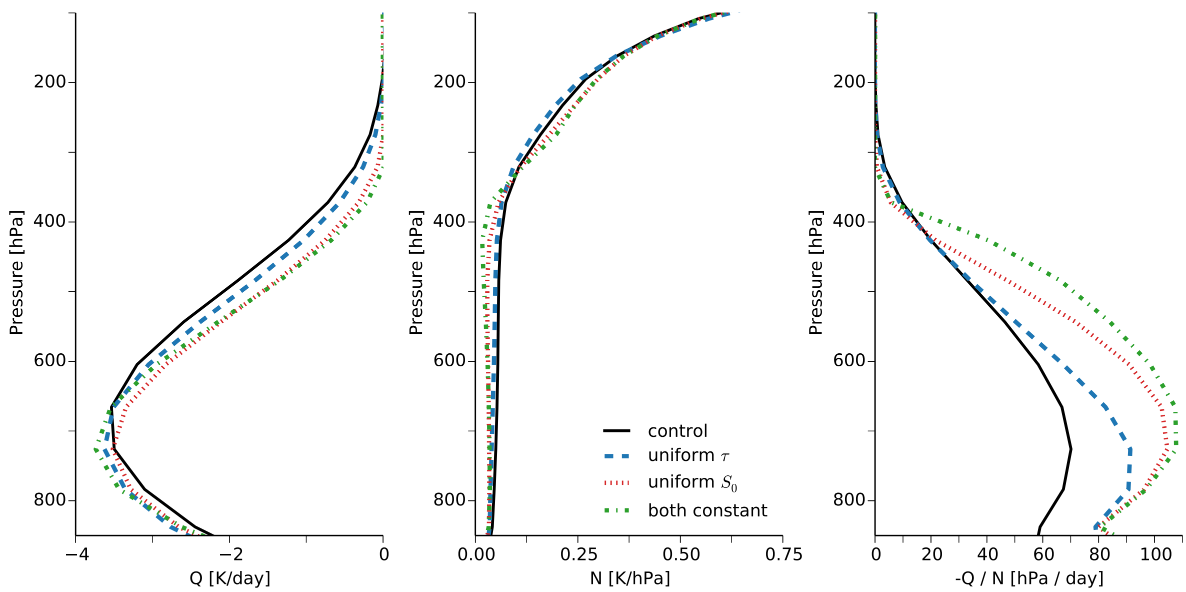

FIG. 5. Global-mean profiles of Q (left panel), N (middle panel) and $-Q/N$ (right panel) for the upper tropospheres and lower stratospheres of the control experiment and the three perturbation experiments.

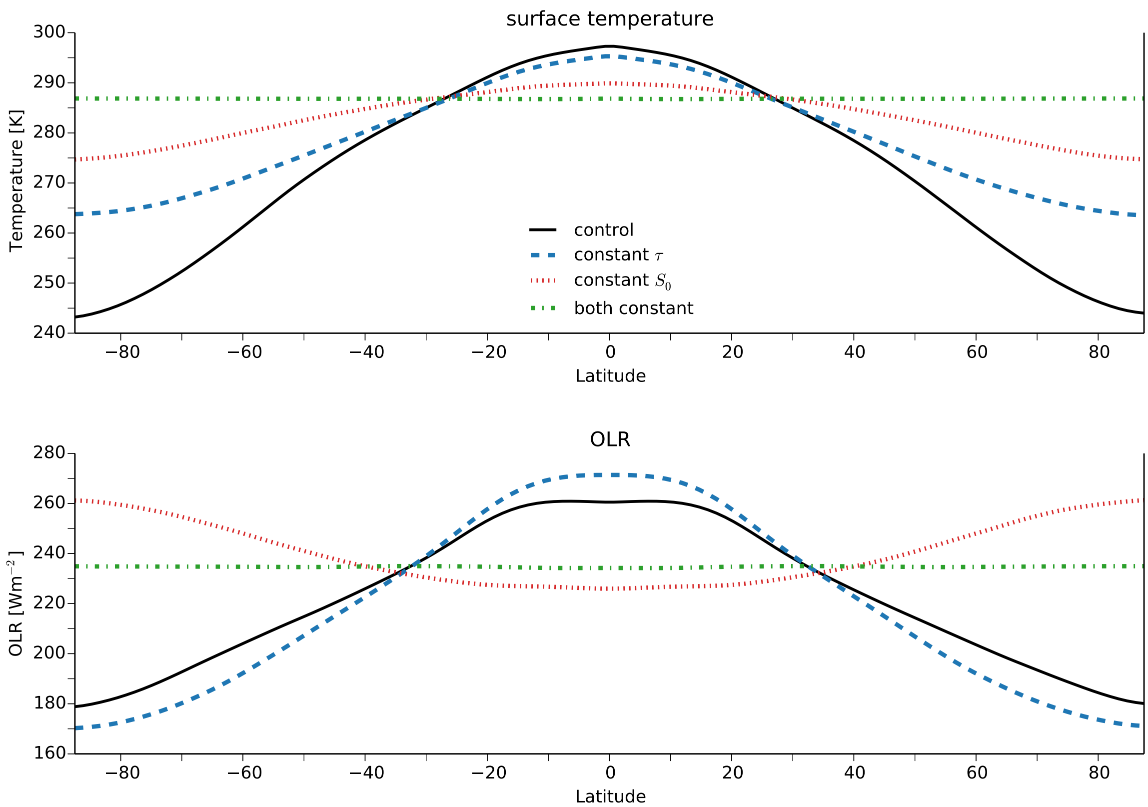

FIG. 6. Top panel: zonal-mean surface temperatures for the control experiment and the three perturbation experiments. Bottom: zonal-mean outgoing long-wave radiation for the same experiments.

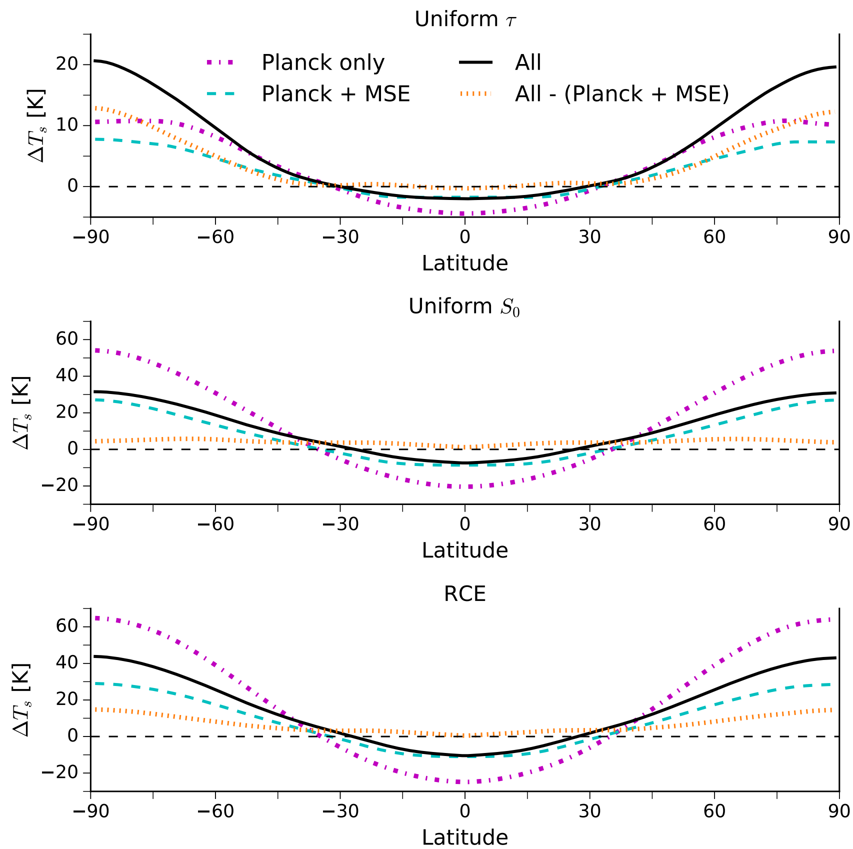

FIG. 7. Top panel: ΔT_s for the uniform τ experiment estimated using just the Planck feedback (magenta dashed line), using the Planck feedback and the change in MSE transport (cyan dashed-dot line) and the actual ΔT_s (solid black line). The orange dotted line shows the actual ΔT_s minus ΔT_s estimated using just the Planck feedback and the change in the MSE transport (i.e., the black line minus the cyan dashed-dot line), a measure of the contribution to ΔT_s by the lapse-rate feedback. Middle panel: same for the uniform S_0 experiment. Bottom panel: same for the RCE experiment.

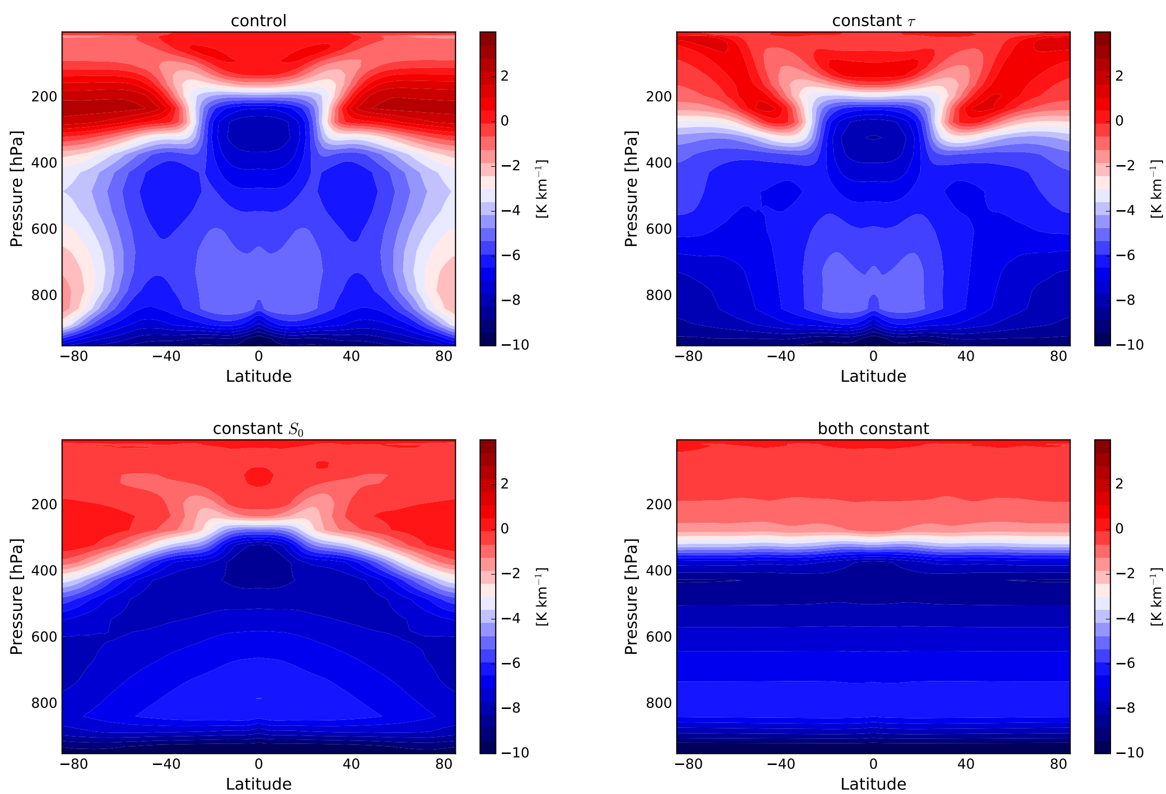

FIG. 8. Zonal-mean lapse-rates in the control experiment and the three perturbation experiments.

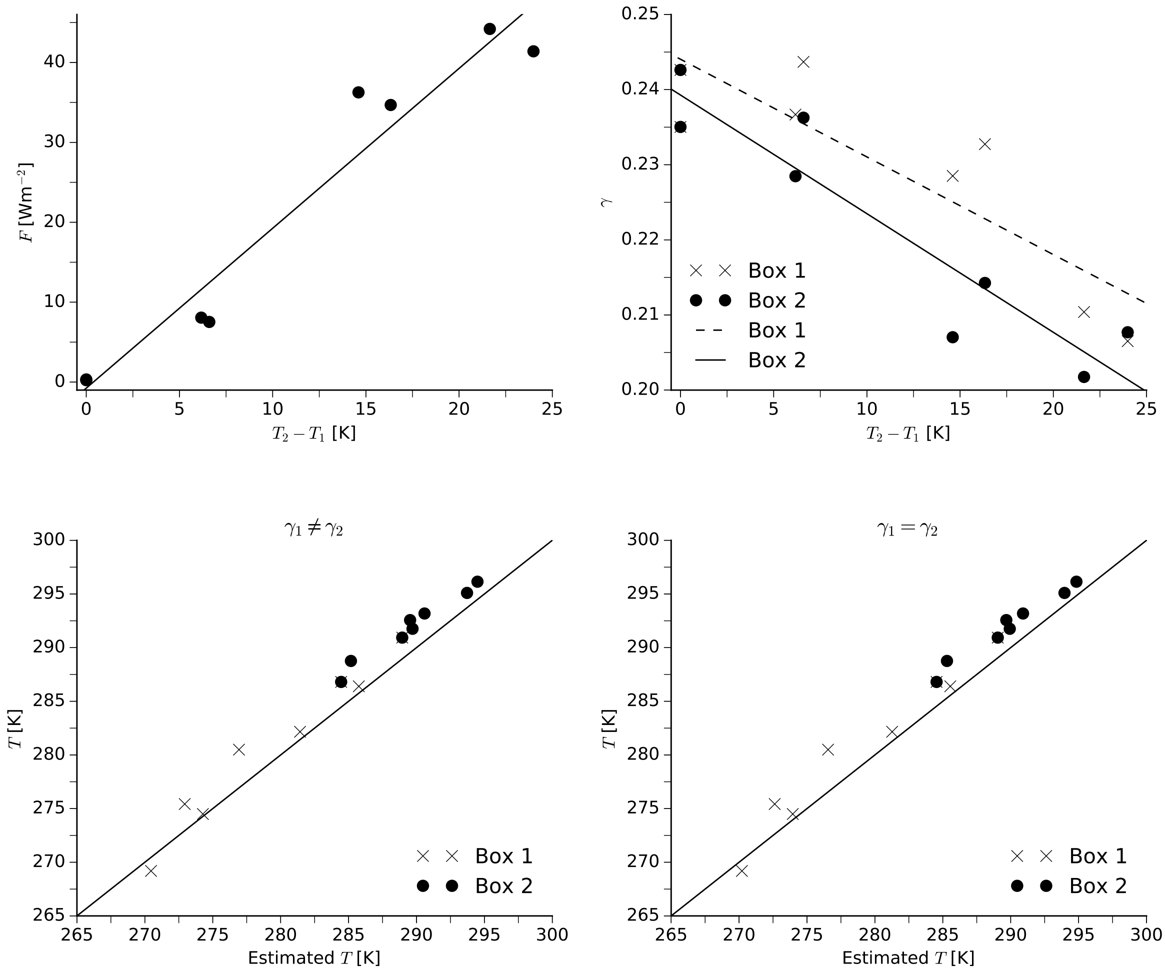

FIG. 9. Top left: energy flux from box 2 into box 1 versus the temperature difference between box 1 and box 2 in the eight simulations with the GCM. Top right: average tropospheric lapse-rate in box 1 (crosses) and box 2 (circles) versus the temperature difference between box 1 and box 2, diagnosed from the eight simulations with the GCM. Bottom left: temperatures in box 1 (crosses) and box 2 (circles) in the GCM versus estimates from the simple model with $\gamma_1 \neq \gamma_2$. Bottom right: temperatures in box 1 (crosses) and box 2 (circles) in the GCM versus estimates from the simple model with $\gamma_1 = \gamma_2$. In the top two panels the lines show linear least-squares regressions of $T_2 - T_1$ versus F (left panel) and γ_1 and γ_2 (right panel). In the bottom panels the lines show the 1:1 lines.

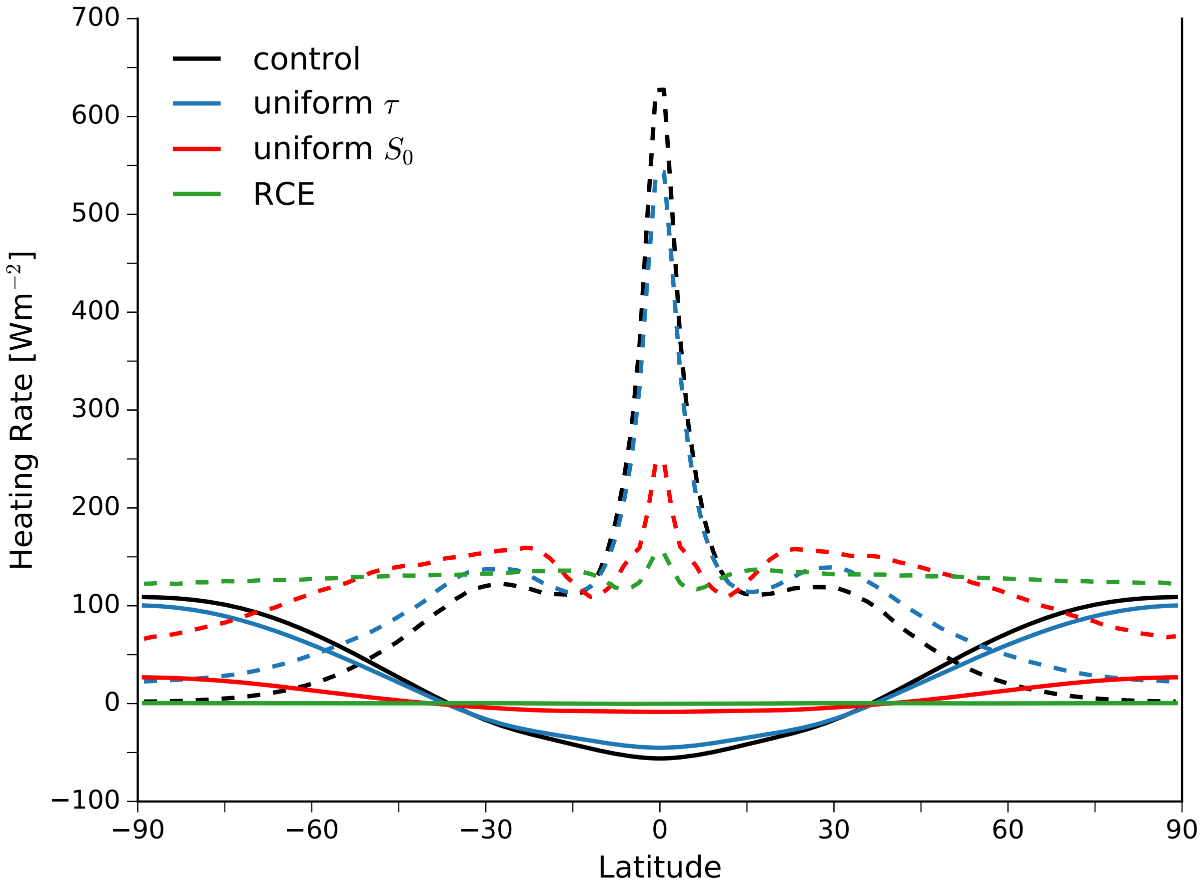

FIG. 10. Zonal-mean vertically-integrated convective heating rates (dashed lines) and convergence of meridional energy fluxes (solid lines) for the control experiment and the three perturbation experiments.

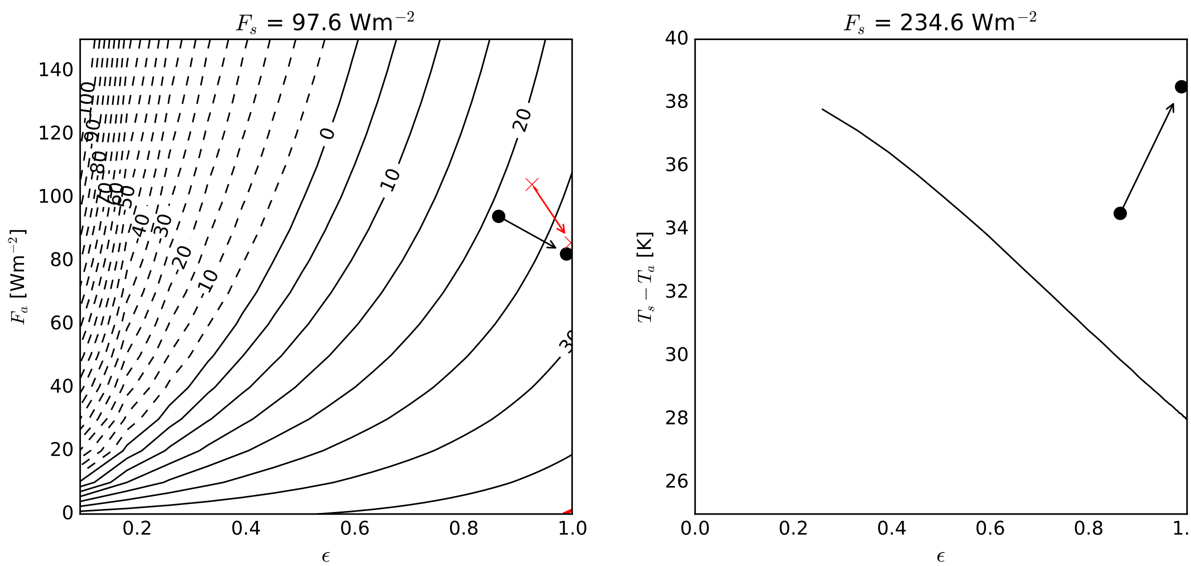

FIG. 11. Left panel: the temperature difference $T_s - T_a$ for a system in RAE and with a mean insolation of 97.6Wm^{-2} as a function of the emissivity and the meridional energy flux, calculated using equations 19a and 19b. The black round markers plot the emissivity and vertically-integrated meridional energy flux, averaged over latitudes polewards of 60°, in the control and uniform τ experiments. The red crosses show the values for the "global-warming" simulations with these set-ups and the red contour in the bottom right hand corner shows the critical temperature difference above which the system becomes unstable to moist convection. Right panel: the critical temperature difference as a function of the emissivity, calculated using a mean insolation of 234.6Wm^{-2}. The two markers plots the temperature differences that would arise in the uniform S_0 and RCE cases if their high latitudes were in RAE, assuming F_a = 100Wm^{-2}.

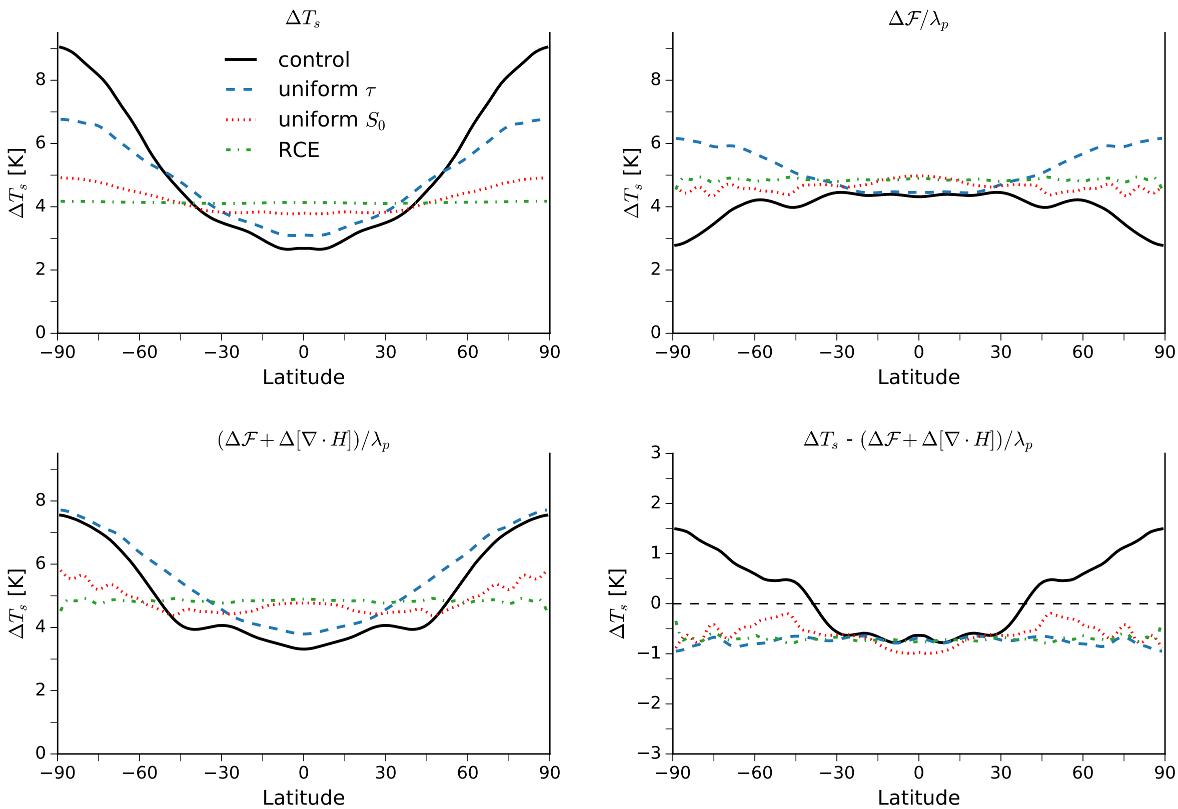

FIG. 12. Top left panel: zonal-mean surface temperature responses in the four global warming experiments. Top right panel: zonal-mean temperature changes due only to the radiative forcing and Planck feedback. Bottom left panel: zonal-mean temperature changes due to the radiative forcing, the change in moist static energy transport and the Planck feedback. Bottom right panel: the differences between the zonal-mean surface temperature responses and the changes due to the radiative forcing, the change in moist static energy transport and the Planck feedback.